

Scaled protogalactic magnetic field generation in laser-produced shock waves

G. Gregori,^{1,2} A. Ravasio,³ C. D. Murphy,¹ K. Schaar,¹ A. Baird,¹ A. R. Bell,¹ A. Benuzzi-Mounaix,³ R. Bingham,² C. Constantin,⁴ R. P. Drake,⁵ M. Edwards,¹ E. T. Everson,⁴ C. D. Gregory,⁶ Y. Kuramitsu,⁷ W. Lau,¹ J. Mithen,¹ C. Niemann,⁴ H.-S. Park,⁸ B. A. Remington,⁸ B. Reville,¹ A. P. L. Robinson,² D. D. Ryutov,⁸ Y. Sakawa,⁷ S. Yang,¹ N. C. Woolsey,⁶ M. Koenig,³ and F. Miniati⁹

¹*Department of Physics, University of Oxford,
Parks Road, Oxford OX1 3PU, UK*

²*Rutherford Appleton Laboratory, Chilton, Didcot OX11 0QX, UK*

³*Laboratoire pour l'Utilisation de Lasers Intenses, UMR7605, CNRS CEA,
Université Paris VI Ecole Polytechnique, 91128 Palaiseau Cedex, France*

⁴*University of California Los Angeles, Los Angeles, CA 90095, USA*

⁵*Atmospheric, Oceanic, Space Science, University of Michigan,
2455 Hayward St, Ann Arbor, MI 48103, USA*

⁶*Department of Physics, Heslington,
University of York, YO10 5DD, UK*

⁷*Institute of Laser Engineering, Osaka University,
2-6 Yamadaoka, Suita, Osaka 565-0871, Japan*

⁸*Lawrence Livermore National Laboratory,
P.O. Box 808, Livermore, California 94551, USA*

⁹*Physics Department, Wolfgang-Pauli-Strasse 27,
ETH-Zürich, CH-8093 Zürich, Switzerland*

The standard model for the origin of galactic magnetic fields is through the amplification of seed fields via dynamo or turbulent processes to the level consistent with current observations [1–3]. While other mechanisms may also operate [4, 5], the Biermann battery inevitably accompanies the formation of galaxies in the absence of a primordial field. Driven by geometrical asymmetries in shocks [6] associated with the collapse of protogalactic structures, it is believed to generate seed fields to a level $\sim 10^{-21}$ G [7, 8]. With the advent of high-power laser systems in the past two decades a new field of research has opened where, using simple scaling relations [9, 10], astrophysical environments can effectively be reproduced in the laboratory [11, 12]. We demonstrate such capability and show experimentally the generation of magnetic seeds by the Biermann effect at protogalactic shocks, consistent with the above findings. Here we report the results of an experiment that produced seed magnetic fields by the Biermann battery effect. We show that these results can be scaled to the intergalactic medium, where turbulence, acting on time-scales ~ 700 Myr, can amplify the seeds fields [13, 14], with significant impact on galaxy evolution.

We conducted these experiments at the LULI 2000 laser facility. The intense laser is used to illuminate a small carbon rod inside a low pressure gas-filled interaction chamber. Full description of the experimental setup, including details on the laser properties, is provided in Fig. 1 and related caption. As energy is impulsively deposited, the heated solid matter initially undergoes a ballistic expansion until the shocked mass is roughly equal to the ejected mass, and then the shock transitions to a Sedov-Taylor blast wave [15, 16]. The shock evolution in time is monitored using optical diagnostics. The experimentally measured shock position for $t \lesssim 200$ ns is then compared with a 1D-radial radiation hydrodynamic simulation using the HELIOS-CR [17] code (Fig. 2). Based on the quantitative agreement in the density values at $t \lesssim 200$ ns, we use the simulations to help interpret the experimental results at later times, $t \sim 0.5\text{-}1.5 \mu\text{s}$, when the shock arrives at the position of the magnetic field probes but the plasma density is below the detection limit of the optical probe.

The measurement of the magnetic field was performed with 3-axis magnetic induction coils [18], giving both the magnetic field components along the shock normal (B_{\parallel}) and perpendicular to it (B_{\perp}), as indicated in Fig. 3. At $r \sim 3$ cm from the initial blast, peak B_{\perp} values occurring at $t \sim 1\text{-}2 \mu\text{s}$ are in the range 10-30 G. The position of the first peak in

B_{\perp} is in agreement with the shock arrival time estimates based on HELIOS-CR, and is also consistent with the time lags between different locations of the probe coils. Finally, shots taken with no ambient gas (not plotted) show no peak in B_{\perp} for $t \sim 0.5\text{-}2 \mu\text{s}$, which further supports the inference that the magnetic field arrives with the shocked plasma.

It is well known that return currents driven by hot electrons can play an important role for field generation in laser produced plasmas [5, 19]. However, at our laser intensity we expect the hot electrons to be distributed with temperature $T_{hot} \sim 5 \text{ keV}$ [20]. So, they would reach the coil position at $t \lesssim 3 \text{ ns}$, much earlier than the measured peak in B_{\perp} . A magnetic field generated through vorticity by Biermann's battery [7] is more plausible. We can estimate it as [21]

$$B_{vort} = \frac{m_i}{e} \omega \approx \frac{(\rho - 1)^2 m_i}{\rho e} \left| \frac{\partial \mathbf{v}_{sh}}{\partial S} \right|, \quad (1)$$

where $\omega = \nabla \times \mathbf{v}$ is the vorticity, m_i is the ion mass, e the electron charge, $\rho \sim 3$ is the shock compression ratio (see Fig. S1) and $\partial \mathbf{v}_{sh}/\partial S$ is the tangential gradient of the shock velocity. Since $\partial v_{sh}/\partial S \sim \kappa v_{sh}/r$, where $\kappa \sim 0.1\text{-}0.3$ (Fig. 3a), at $r \sim 3 \text{ cm}$ we find $B_{vort} \approx 10\text{-}30 \text{ G}$, in agreement with the measured values. The range of measured magnetic field strengths agrees with the observed shot-to-shot variations in the measured shock properties at early times, as indicated in the Supplementary Information. We observe that the peak of the measured magnetic energy density in the downstream plasma corresponds to a fraction of a percent of that of the incoming flow, *i.e.*, $\epsilon_B = B^2/\mu_0 n_g^0 m_i v_{sh}^2 \approx 0.1\%$, where n_g^0 is the upstream gas density (Fig. S1). On the other hand, the magnetic field energy density is significantly larger than the ram pressure of the incoming ionized plasma, *i.e.*, $\epsilon_B^i = B^2/\mu_0 n_e^0 m_i v_{sh}^2 \gtrsim 0.1$ (with $n_e^0 \sim 10^{14} \text{ cm}^{-3}$ the inferred electron density ahead of the shock). This suggests that, in this experiment, the kinetic Weibel instability may not play a significant role, as one would expect it to produce a much smaller field, *i.e.*, $\epsilon_B^i \sim (m_e/m_i) \approx 10^{-3}$ [4, 22], where m_e is the electron mass.

The vorticity generated field is perpendicular to the shock normal, consistent with the experimental traces of Fig. 3 that show $B_{\perp} \gg B_{\parallel}$. We notice that in a perfectly spherical shock no magnetic field can be produced since $\partial v_{sh}/\partial S = 0$. Magnetic fields can thus only be generated in non spherical expansion shocks, which are expected to occur during structure formation in the pregalactic era [7]. Our interpretation is reinforced by a computer calculation which solves the resistive magneto-hydrodynamics (MHD) equations in

2-dimensions (Fig. 4) with a baroclinic source term for the magnetic field generation (i.e., $-\nabla n_e \times \nabla p_e / en_e^2$, with n_e the electron density and p_e the electron pressure). The asymmetric expansion due to the initial temperature anisotropy of the laser illumination drives baroclinic generation of a magnetic field comparable in strength to what is measured in the laboratory.

We have applied the MHD scaling techniques to investigate the importance of the Biermann battery for magnetic field generation at high Mach number astrophysical shocks occurring in the intergalactic medium (IGM). Similarity in the MHD equations is preserved if heat convection over conduction (the Peclet number), inertial forces over viscosity (the Reynolds number), as well as the ratio of inertial forces over magnetic diffusivity (the magnetic Reynolds number) are all large in both systems (Table I). From Eq. 1, the magnetic field generated by the Biermann mechanism is proportional to the shock generated vorticity. It follows that, on a spatial scale ℓ , $\omega \sim v_{sh}/\ell \sim 1/t$ (see also Supplementary Information). Our laboratory results thus indicate that curved intergalactic shocks in protogalactic structures, with changing curvature at the level of a few tens of a percent on scales ~ 1 Mpc, can generate magnetic field with values $\sim 10^{-21}$ G. Both the curvature radius, the asymmetry and the resulting magnetic field, are consistent with the scenario of protogalactic magnetic field generation from the Biermann battery process modeled with numerical simulations in Ref. [7]. This is an important experimental verification of such process. Generation of these tiny magnetic fields precedes the formation of the galaxy. This is significant in that the magnetic field can be quickly amplified to about equipartition values by turbulent motions and can have important role on the evolution of the the galactic medium from its early stages [13, 14]. Indeed, astronomical observations show that dynamically strong magnetic fields are common even in young galaxies [25, 26]. The excellent agreement between the experiment and current theories of magnetic field generation in the early universe opens an exciting range of possibilities, where other effects that may influence the generation of seed fields can be accurately modeled in the laboratory.

[1] Parker, E. N., Hydromagnetic dynamo models. *Astrophys. J.* **122**, 293-314 (1955).

[2] Zweibel, E. G., and Heiles, C., Magnetic fields in galaxies and beyond. *Nature* **385**, 131-136

- (1997).
- [3] Ryu, D., Kang, H., Cho, J., and Das, S., Turbulence and magnetic fields in the large-scale structure of the universe. *Science* **320**, 909-912 (2008).
 - [4] Schlickeiser R., and Shukla, P. K., Cosmological magnetic field generation by the Weibel instability. *Astrophys. J.* 599, L57-60 (2003).
 - [5] Miniati, F., and Bell, A. R., Resistive magnetic field generation at cosmic dawn. *Astrophys. J.* **729**, 73 (2011).
 - [6] Miniati, F., *et al.*, Properties of cosmic shock waves in large-scale structure formation. *Astrophys. J.* **542**, 608-621 (2000).
 - [7] Kulsrud, R. M., Cen, R., Ostriker, J. P., and Ryu, D., The protogalactic origin for cosmic magnetic fields. *Astrophys. J.* **480**, 481-491 (1997).
 - [8] Xu, H., *et al.*, The Biermann battery in cosmological MHD simulations of population III star formation. *Astrophys. J.* **688**, L57-60 (1957).
 - [9] Ryutov, D. D., *et al.*, Similarity criteria for the laboratory simulation of supernova hydrodynamics. *Astrophys. J.* **518**, 821-832 (1999).
 - [10] Ryutov, D. D., Drake, R. P., and Remington, B. A., Criteria for scaled laboratory simulations of astrophysical MHD phenomena. *Astrophys. J.* **127**, S465-468 (2000).
 - [11] Remington, B. A., Arnett, D., Drake, R. P., and Takabe, H., Modeling astrophysical phenomena in the laboratory with intense lasers. *Science* **284**, 1488-1493 (1999).
 - [12] Remington, B. A., Drake, R. P., and Ryutov, D. D., Experimental astrophysics with high power lasers and Z pinches. *Rev. Mod. Phys.* **78**, 755-807 (2006).
 - [13] Cho, J., and Vishniac, E. T., The generation of magnetic fields through driven turbulence. *Astrophys. J.* **538**, 217 (2000).
 - [14] Sur S., Schleicher D. R. G., Banerjee R., Federrath C., Klessen R. S., The generation of strong magnetic fields during the formation of the first stars. *Astrophys. J.* **721**, L134-138 (2010).
 - [15] Hansen, J. F., *et al.*, Laboratory simulations of supernova shockwave propagation. *Astrophys. Space Sci.* **298**, 61-67 (2005).
 - [16] Hansen, J. F., *et al.*, Laboratory observation of secondary shock formation ahead of a strongly radiative blast wave. *Phys. Plasmas* **13**, 022105 (2006).
 - [17] MacFarlane, J. J., Golovkin, I. E., and Woodruff, P. R., HELIOS-CR - a 1-D radiation-magnetohydrodynamics code with inline atomic kinetics modeling. *J. Quant. Spect. Radiat.*

- Transfer **99**, 381-397 (2006).
- [18] Everson, E. T., *et al.*, Design, construction, and calibration of a three-axis, high-frequency magnetic probe (B-dot probe) as a diagnostic for exploding plasmas. *Rev. Sci. Instrum.* **80**, 113505 (2009).
- [19] Bell, A. R., and Kingham, R. J., Resistive collimation of electron beams in laser-produced plasmas. *Phys. Rev. Lett.* **91**, 035003 (2003).
- [20] Reich, Ch., Gibbon, P., Uschmann, I., and Föster, E., Yield optimization and time structure of femtosecond laser plasma $K\alpha$ sources. *Phys. Rev. Lett.* **84**, 4846-4849 (2000).
- [21] Hayes, W. D., The vorticity jump across a gasdynamic discontinuity. *J. Fluid Mech.* **2**, 595-600 (1957).
- [22] Medvedev, M. V., Weibel turbulence in laboratory experiments and GRB/SN shocks. *Astrophys. Space. Sci.* **307**, 245-250 (2007).
- [23] Ziegler, U., A central-constrained transport scheme for ideal magnetohydrodynamics. *J. Comp. Phys.* **196**, 393-416 (2004).
- [24] Ya. B. Zel'dovich and Yu. P. Raizer, *Physics of shock waves and high-temperature hydrodynamic phenomena.* (Academic, New York, 1966).
- [25] Bernet, M. L., Miniati, F., Lilly, S. J., Kronberg, P. P., and Dessauges-Zavadsky, M., Strong magnetic fields in normal galaxies at high redshift. *Nature* **454**, 302-304 (2008)
- [26] Murphy E. J., The far-infrared-radio correlation at high redshifts: physical considerations and prospects for the square kilometer array. *Astrophys. J.* **706**, 482-496 (2009).

Acknowledgements

We thank the LULI technical team for their support during the experiments. The research leading to these results has received funding from the European Research Council under the European Community's Seventh Framework Programme. This work was also supported by the EU program Laserlab-Europe. Partial support from the Science and Technology Facilities Council and the Engineering and Physical Sciences Research Council of the United Kingdom is also acknowledged.

Author Contributions

G.G. and F.M. have conceived this project. G.G., A.R., C.D.M., A.B.-M., M.E., C.D.G., Y.K., J.M., H.-S.P., N.C.W. and M.K. carried out the LULI experiment. The paper was written by G.G., A.R., A.R.B., R.P.D., B.R. and F.M. The data was analyzed by G.G., A.R., C.D.M., K.S., and C.D.G. Preparatory diagnostics work was conducted by A.B., C.C., E.T.E., C.N., W.L., and S.Y. Numerical simulations were performed by G.G. and A.P.L.R. Additional experimental and theoretical support was provided by A.R.B., R.B., R.P.D., B.A.R., B.R., D.D.R., Y.S. and F.M.

Author Information

Reprints and permissions information is available at www.nature.com/reprints. The authors declare no competing financial interests. Correspondence and requests for materials should be addressed to g.gregori1@physics.ox.ac.uk (G. Gregori), or fm@phys.ethz.ch (F. Miniati).

Figure captions

FIG. 1: Experimental setup showing the laser beams and diagnostics configuration. Either one or two frequency-doubled (527 nm), 1.5 ns-long laser beams are focussed on the tip of a 500 μm diameter carbon rod. At focus, each laser beam has a 400 μm flat-top distribution achieving a peak intensity of 2×10^{14} W/cm², delivering ~ 350 J. The interaction chamber is filled with helium gas at pressure $p = 0.8 \pm 0.3$ mbar or $p = 1.6 \pm 0.3$ mbar. The shock wave evolution during times $t \lesssim 200$ ns (where $t = 0$ corresponds to the time of the laser pulse) was monitored using transverse interferometry and Schlieren/shadowgraphy with an optical probe (with 532 nm wavelength and 6 ns gate width). The interferometer was of Mach-Zehnder type with ~ 25 mm field of view, and it was used to provide the electron density. The inset on the left shows an example of an interferometric image. The inset on the right shows a streaked self-emission optical pyrometry (SOP) image in a narrow band at 450 ± 30 nm.

FIG. 2: Comparison between numerical simulations and optical diagnostics. (a) HELIOS-CR simulations (done with one beam laser driver) and experimentally determined shock position with both interferometry and SOP. The laser energy deposition in the HELIOS-CR code was adjusted to 70% of the nominal value to have the simulated shock position match the experimental values. The transition to a Sedov-Taylor blast wave occurs at distances $r < 10$ mm from the sample. (b) Calculated electron density at $t = 150$ ns *vs* electron density values extracted from interferometric measurements via Abel inversion, which requires the assumption of cylindrical symmetry. Since observed differences in the shock wave radius are less than 20%, this gives the uncertainty in the density measurement.

FIG. 3: Magnetic field measurements from induction coils. (a) Schlieren image showing laser and magnetic pick-up coil configuration as well as the shock position. The Schlieren image indicates when the refractive index of the plasma changes rapidly, thus tracking the position of the shock. From the asymmetry in the shape of the shock wave we approximate $\kappa \sim 0.1-0.3$ in Eq. (1). The induction coils are placed at 2.8 cm and 3.6 cm from the carbon rod (*i.e.*, the center of the initial blast). Each coil consists of 8 twisted pairs coils wound around the axis of a $\sim 3.1 \times 3.1$ mm² plastic core. The voltage from the twisted pair loops is then differentially amplified in order to remove any electric field components, and the magnetic field is calculated using Faraday's law. The coils are protected from the surrounding plasma by a 1 mm thick glass tube. Time resolution is better than 50 ns. We estimated the error associated to each magnetic field trace to be $\sim 15\%$. The rise and gradual decay of B_{\perp} is consistent with the shock front crossing the coil and the subsequent evolution of the shocked material. The second peak at $t \sim 5$ μ s seen for the case of two beams illumination is likely associated to the ejecta material from the sample arriving at the coil. (b) B_{\perp} (lines) and B_{\parallel} (symbols) traces taken at $p = 0.8$ mbar. (c) B_{\perp} (lines) and B_{\parallel} (symbols) traces for one beam laser driver at $p = 1.6$ mbar. (d) Same as (b) but at $r = 3.6$ cm. The inset shows the measured shock radius along the laser axis for $p = 0.8$ mbar and single beam illumination. We attribute shot-to-shot variations in the observed field values (up to $\sim 50\%$) to the stochastic generation of vorticity and to variations in the radius of curvature of the shock front (as large as $\sim 20\%$ at early times, as shown in the inset).

FIG. 4: Resistive MHD simulations of the magnetic field generation. The MHD scheme is an implementation of Ref. [23]. The ionization state is computed using Saha equilibrium [24]. Radiation transport, thermal conduction and laser coupling were not included in the MHD code. While radiation transport is important during the early stages of the laser drive (for a few ns), at the time when the shock has expanded and magnetic field measurements are taken, the radiation cooling time exceeds the hydrodynamic time scale ($\tau_{rad}/\tau_{hydro} \sim 8 \times 10^3$), thus radiative processes will not affect the hydrodynamic evolution. For the initial conditions we use the results from HELIOS-CR. At $t = 150$ ns (*i.e.*, the time when the shock has swept ~ 1 cm from the initial carbon rod position), the system has uniform density and temperature, except for a central region ($r < 1$ cm) where the temperature is, $T(x, y) = T_0 (1 + \delta \cos \theta)$, with $T_0 = 50$ eV and $\delta = 0.9$, and $\theta \in [0, 2\pi]$ the polar angle. Thus the scale coefficient $\kappa \sim 1/\pi$, in agreement with experimental estimates. The numerical grid consists of 2000×2000 cells with resolution $\Delta x = \Delta y = 0.005$ cm. (a) 2D plot of the perpendicular component of the magnetic field obtained from MHD simulations. Note that because of finite magnetic diffusion, the plasma is magnetized ahead of the shock front. (b) Plot of the magnetic flux density at 2.7 cm from the center of the domain ($x = 2.5$ cm, $y = 1$ cm).

TABLE I: Similarity scaling between the laboratory and the IGM. The similarity between the astrophysical and the laboratory systems breaks down due to viscous dissipation at laboratory scales $h \lesssim \lambda_{coll}$, where λ_{coll} is the collisional mean free path [9], and equally for thermal and magnetic dissipation. This implies that, for the conditions of our experiment, for which magnetic dissipation is the dominant effect, full similarity is achieved at macroscopic scales ($h \gtrsim 5 \mu\text{m}$), while the microphysics at the kinetic level will be different. The similarity given here roughly applies to the shocked IGM for scales $L \gtrsim 25 \text{ pc}$.

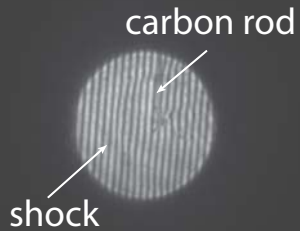
Scaling parameters	Definition	Laboratory (LULI)	IGM
Length	$L \sim 2r/\kappa$	18.8 cm	1 Mpc
Time	t	1 μs	0.7 Gyr
Electron temperature	T_e	2 eV	100 eV
Electron density	n_e	$5 \times 10^{15} \text{ cm}^{-3}$	10^{-4} cm^{-3}
Cyclotron frequency	$\Omega_B = \frac{eB}{m_i}$	$4.8 \times 10^4 \text{ s}^{-1}$	$8.7 \times 10^{-18} \text{ s}^{-1}$
Reynolds number	Re	7.9×10^3	3.0×10^{13}
Peclet number	Pe	69.0	7.0×10^{11}
Magnetic Reynolds number	Re _M	16.5	3.9×10^{27}

Beam north
350 J

Beam south
350 J

Interferometry

$t=100$ ns



3 axis
induction coil

B_{\perp}

$B_{||}$

SOP

probe beam:
Interferometry
Shadowgraphy

carbon rod

SOP

